



**CHALMERS**  
UNIVERSITY OF TECHNOLOGY

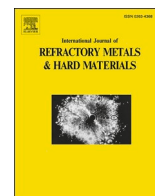
## **Schmid factor analysis for chip flow induced plastic deformation of textured cubic carbonitride coatings**

Downloaded from: <https://research.chalmers.se>, 2024-04-25 17:34 UTC

Citation for the original published paper (version of record):

Qiu, R., Shoja, S., von Fieandt, L. et al (2022). Schmid factor analysis for chip flow induced plastic deformation of textured cubic carbonitride coatings. International Journal of Refractory Metals and Hard Materials, 108.  
<http://dx.doi.org/10.1016/j.ijrmhm.2022.105932>

N.B. When citing this work, cite the original published paper.



# Schmid factor analysis for chip flow induced plastic deformation of textured cubic carbonitride coatings

Ren Qiu<sup>a,\*</sup>, Siamak Shoja<sup>a,b</sup>, Linus von Fieandt<sup>b</sup>, Jan Engqvist<sup>b</sup>, Olof Bäcké<sup>a</sup>,  
Hans-Olof Andrén<sup>a</sup>, Mats Halvarsson<sup>a</sup>

<sup>a</sup> Department of Physics, Chalmers University of Technology, SE-412 96 Gothenburg, Sweden

<sup>b</sup> Sandvik Coromant, SE-126 79 Hägersten, Sweden

## ARTICLE INFO

### Keywords:

CVD  
Ti(C,N)  
Hard coatings  
Schmid factor  
Deformation mechanism

## ABSTRACT

In high-speed metal machining, cutting tools in the form of cemented carbide inserts coated with thin wear-resistant coatings are commonly used. These coatings are often made of metal carbonitrides with cubic rock salt crystal structure and different growth textures. However, the influence of the crystallographic texture of the coatings on their wear by plastic deformation due to the chip flow during machining needs to be revealed further. In this work, in order to analyse the ability of polycrystalline fibre-textured coatings with a rock salt structure to undergo plastic deformation, a method was developed for calculating Schmid factors of such textured coatings as a function of the loading angle of an external force. The Schmid factors were calculated for coatings with 100 and 211 growth textures, and {100} <110>, {110} <110> and {111} <110> as possible slip systems. For the {111} <110> slip systems, the Schmid factors are not much influenced by the force angle and coating texture, which is contrary to the {100} <110> and {110} <110> slip systems. The simulations were compared to wear on the rake face of two textured Ti(C,N) coatings after short longitudinal turning tests. The variation of the degree of plastic deformation of Ti(C,N) coatings with growth texture and external force angle indicates that the dominant activated slip systems are {110} <110> using the machining conditions applied in this work.

## 1. Introduction

Cutting tool inserts for high-speed metal machining need to withstand extreme pressures and thermal loads. Thus, such inserts are commonly made of cemented carbide (a composite material based on tungsten carbide (WC) and Co) that exhibits both good toughness and hardness [1,2]. The cutting performance of cemented carbide inserts can be improved through depositing thin wear-resistant coatings with higher hardness onto them, and research has been focused on synthesizing new wear-resistant coatings for machining advanced materials used by modern industry. In recent years, wear-resistant coatings with strong growth textures (and columnar grain morphologies) have been synthesized via chemical vapour deposition (CVD) and physical vapour deposition (PVD) [3–19], and the textured coatings have been reported to show significantly improved cutting performance [8,11].

Wear-resistant coatings are usually made of hard materials, which can be brittle and easy to fracture at room temperature. However, at the higher temperatures occurring during cutting operations, where the

coatings transition from being brittle to being ductile, plastic deformation has been found to occur [8,20,21]. The coating temperature depends on the details of the cutting operation, but can frequently reach 600–950 °C locally in the area of contact between the coating and the workpiece material [7]. Ruppert et al. proposed that plastic deformation of  $\alpha$ -Al<sub>2</sub>O<sub>3</sub> coatings during metal machining reduces cracking and flaking, factors important for the total wear [8]. Therefore, the capability of plastic deformation of these wear-resistant coatings is believed to be essential for their good cutting performance.

Commonly used wear-resistant coatings include metal nitrides and carbides with rock salt crystal structures, such as TiN [5,19], (Ti,Al)N [3,12–14,17,18,22,23], Ti(C,N) [6,15,24], and oxides, such as  $\alpha$ -Al<sub>2</sub>O<sub>3</sub> (corundum structure, trigonal) [4,7–9] and  $\kappa$ -Al<sub>2</sub>O<sub>3</sub> (orthorhombic structure) [10,25–27]. In addition, wear-resistant coatings can be grown with different fibre textures, which means that the grains are randomly rotated around an axis along the coating normal, while having the same orientation (texture) along the coating normal. Typical fibre textures include 111 [12–15,24,28], 211 [15,24,29], and 100 [30] for the rock

\* Corresponding author.

E-mail address: [renq@chalmers.se](mailto:renq@chalmers.se) (R. Qiu).

<https://doi.org/10.1016/j.ijrmhm.2022.105932>

Received 8 April 2022; Received in revised form 31 May 2022; Accepted 14 June 2022

Available online 17 June 2022

0263-4368/© 2022 The Author(s). Published by Elsevier Ltd. This is an open access article under the CC BY license (<http://creativecommons.org/licenses/by/4.0/>).

salt structured carbides and nitrides, and 0001, 01 $\bar{1}2$ , and 11 $\bar{2}0$  for the trigonal  $\alpha$ -Al<sub>2</sub>O<sub>3</sub> [9].

Ruppi et al. studied the wear-resistance of  $\alpha$ -Al<sub>2</sub>O<sub>3</sub> coatings with different textures, and concluded that 0001 textured  $\alpha$ -Al<sub>2</sub>O<sub>3</sub> coatings exhibit less wear due to plastic deformation accommodated by easier basal (0001) slip [8]. It was suggested that the texture of these coatings influenced the plastic deformation (from chip flow) due to the specific orientation of the slip systems (slip plane and slip direction) with respect to the direction of the resulting force on the coatings during the metal machining process [8]. Accordingly, Shoja et al. proposed a method for modelling Schmid factors of  $\alpha$ -Al<sub>2</sub>O<sub>3</sub> coatings with specific growth textures and different slip systems (basal and prismatic slip systems) with respect to the direction of the loading force, and correlated the simulated results with the microstructure, surface topography and wear of the worn CVD  $\alpha$ -Al<sub>2</sub>O<sub>3</sub> coatings in different wear areas on the rake face of the cutting tool insert with different resulting force angles [9]. However, the ability of cubic metal nitride and carbide coatings with different growth textures to undergo plastic deformation has not been equally explored. Therefore, the scope of this paper is to generalize the methodology of Schmid factor simulations proposed by Shoja et al. to coatings with rock salt structure, and evaluate their ability for plastic deformation coupled to their texture and the loading force angle, i.e. the wear zone of the tool insert.

The probable slip systems for rock salt structure are {100} <110>, {110} <110> and {111} <110> (the Burgers vectors are  $\frac{1}{2}$  <110>, but the ' $\frac{1}{2}$ ' is ignored in the notation of slip system in this work for simplicity), depending on the material and temperature at which the deformation occurs [31–40]. It should be noted that the correlation between temperature and activated slip system has not been fully revealed for many of the cubic nitrides and carbides that are commonly used as wear-resistant coatings (such as TiN, Ti(C,N), (Ti,Al)N).

The aim of this work is to understand the influence of the coating texture, the slip systems, and the angle of the force resulting from the chip flow during a metal machining process on the ability of plastic deformation of hard cubic carbonitride coatings with a rock salt structure. Accordingly, the Schmid factors of these coatings, as a function of the loading force angles, slip systems and coating textures, were calculated. In addition, CVD wear-resistant coatings of Ti(C,N) were deposited on cemented carbide cutting tool inserts with either a 100 or a 211 texture. After deposition, the coatings were exposed to a short turning test. The microstructures of as-deposited coatings, as well as worn coatings at different areas on the inserts (corresponding to different loading force angles) were investigated by scanning electron microscopy (SEM) and complementary electron backscattered diffraction (EBSD). The influence of the texture and force angle on the surface topography and ability of plastic deformation was then correlated to the Schmid factor simulations.

## 2. Materials and methods

### 2.1. CVD synthesis of the Ti(C,N) coatings

The cutting tools used in this study were indexable cemented carbide inserts of CNMG120408-PM geometry. The composition of the cemented carbide was 7.2 wt% Co, 2.9 wt% TaC, 0.5 wt% NbC, 1.9 wt% TiC, 0.4 wt% TiN, the remainder being WC. The CVD depositions were carried out in an industrial scale CVD reactor (Bernex 530 type) where the inserts were placed in the middle of the reactor at the half-radius of the coating tray (middle position). Either 100 or 211 textured Ti(C,N) coatings were deposited onto inner 0.3  $\mu$ m thick TiN coatings, according to the data in Table 1. All depositions were carried out at a temperature of 885 °C. The produced Ti(C,N) coatings were between 11 and 17  $\mu$ m thick.

**Table 1**

Deposition parameters for the CVD coatings (100 and 211 textured Ti(C,N) layers, denoted as (100) Ti(C,N) and (211) Ti(C,N), respectively, and the inner TiN layer), partial pressures (in kPa) for each precursor, and total pressure (kPa) in the reactor. The temperature was 885 °C in all cases.

Layer/precursor data	H <sub>2</sub>	N <sub>2</sub>	HCl	TiCl <sub>4</sub>	CH <sub>3</sub> CN	Total pressure
(100) Ti(C,N)	3.0	3.0	0.75	0.10	0.15	7.0
(211) Ti(C,N): step I	3.2	2.1	0.00	0.16	0.025	5.5
(211) Ti(C,N): step II	4.5	0.43	0.43	0.13	0.036	5.5
Inner TiN	19.5	19.5	0.00	0.98	0.00	40

### 2.2. Metal machining

The machining tests were carried out using a bearing steel workpiece material (100CrMo7–3) in a modern CNC lathe. The main constituents of the workpiece material were (in wt%) C 0.96, Si 0.26, Mn 0.67, Cr 1.67, Ni 0.15, Mo 0.23, Al 0.34 and Fe (balance). The samples were machined using longitudinal turning for 1 min. The cutting speed was 220 m/min, the feed was 0.3 mm/revolution, the depth of cut was 2 mm. A water miscible cutting fluid was used as coolant.

### 2.3. Electron microscopy and Schmid factor simulation

A Zeiss Ultra 55 field emission gun SEM with a secondary electron detector was used for plan view and cross sectional imaging of both the as-deposited and worn Ti(C,N) coatings. An FEI Versa 3D focused ion beam (FIB) – SEM equipment was used to polish the top surface of the as-deposited coatings for plan view EBSD measurements. A TESCAN GAIA3 FIB-SEM instrument equipped with an Oxford NanoNordlys detector was used for the EBSD experiments. The EBSD data was analysed by the MTEX tool box in MATLAB [41]. The simulation of the Schmid factors were performed using built-in functions of MTEX [41].

## 3. Results

### 3.1. Plastic deformation of the textured Ti(C,N) coatings

The normal and shear stresses over the rake face of a cutting tool insert during machining varies (both the total magnitude and the ratio between these two types of stress) and the rake face is often divided into three different wear zones: sticking zone (I), transition zone (II) and sliding zone (III). The normal stress is dominant at the edge of the insert and decreases towards the end of the contact length (with the workpiece material) and the shear stress has a maximum value around the middle of the contact length [7]. Thus, the inclination angle of the resulting external force during the metal machining process varies spatially over the rake face of the cutting tool insert.

As has been reported [7,9], the inclination angle of the resulting force gradually increases from 10° (with respect to the coating normal) in zone I to around 45° at the border between the transition and sliding zones (denoted as zone II/III), as schematically illustrated in Fig. 1. For a coating with a strong growth texture, its capability for (local) plastic deformation depends significantly on the inclination angle of the resulting force, because the local Schmid factor is influenced by the angle between the force and the orientation of the slip systems (slip plane normal and slip direction), which varies with crystal orientation (texture), as will be explained in more detail in Section 3.2.

In this work the deformation of two Ti(C,N) coatings, with 100 and 211 textures, was studied. Fig. 2 (a) and (b) show the plan view SEM micrographs of the Ti(C,N) coatings with 100 and 211 textures, respectively. The coatings have similar grain size (below 2  $\mu$ m) according to their surface morphologies. Fig. 2 (c) and (d) show the fracture cross sectional SEM micrographs of the Ti(C,N) coatings with 100 and 211 textures, respectively. The textures of these two Ti(C,N) coatings were verified using plan view EBSD analysis. Fig. 2 (e) and (f) show

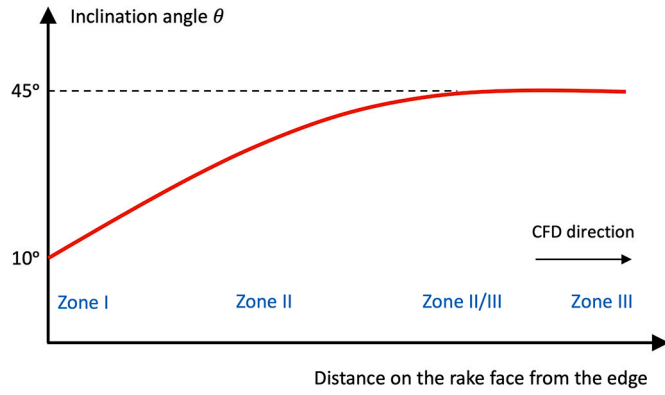


Fig. 1. Schematic drawing showing the variation of the inclination angle of the resulting force over the different wear zones (I, II and III) on the rake face of an insert due to the chip flow during the metal machining process. The chip flow direction (CFD) and wear zones are indicated.

the inverse pole figure (IPF) maps plotted for the coating normal direction (out of plane) for the 100 and 211 textured Ti(C,N), respectively. Fig. 2 (g) displays the colour legend for the IPF maps. Most of the grains shown in Fig. 2 (e) are coloured red, which indicates a 100 texture, while most of the grains shown in Fig. 2 (f) are purple, corresponding to a 211 texture. This coincides with the IPF results, as shown in Fig. 2 (h) and (i). In addition, both coatings were found to have fibre textures as expected.

The surface topography due to the chip flow on the rake face of the coated inserts after the metal machining for 1 min is shown in Fig. 3. The presence of features such as the elongated ridges in the SEM micrographs indicates that the coatings have undergone plastic deformation.

For the 100 textured coating, the elongation of grains can be recognized in zone I, as shown in Fig. 3 (a). Moving to zone II, the plastic deformation of grains becomes more significant, see Fig. 3 (b). This is due to a larger magnitude of the total stress and a corresponding higher temperature in zone II than in zone I [7]. However, moving from (the middle of) zone II to zone II/III, see Fig. 3 (c), it seems that the grains could not be elongated anymore and therefore got truncated and retained some remnants of the original surface morphology, mainly perpendicular to the chip flow. They were not as elongated as the grains in the 211 textured coating, see Fig. 3 (f).

For the 211 textured coating, no obvious deformation of grains can be recognized in zone I, see Fig. 3 (d). In zone II, the grains are clearly elongated, see Fig. 3 (e). In zone II/III, the elongation of some of the grains becomes larger and as a result, long ridges can be observed, and most of the original surface morphology is gone, as shown in Fig. 3 (f).

It is also worth noting that the grains in the 100 textured coating exhibits more deformation than the 211 textured coating in zone I (see Fig. 3 (a) and (d)), and the 211 textured coating is more deformed than the 100 textured coating in zone II/III (see Fig. 3 (b) and (e)). In zone II, the extent of elongation of grains is similar for the two coatings, (see Fig. 3 (c) and (f)). In addition, the smallest and largest elongation of grains happens in zone I (see Fig. 3 (d)) and zone II/III (see Fig. 3 (f)) of the 211 textured coating, respectively.

To summarize, in zone I, the 100 textured coating shows more deformation; in zone II, similar deformation was observed for the two textures; in zone II/III, the 211 textured coating exhibits a more significant and non-uniform deformation, where some grains were deformed more heavily, while the 100 textured coating shows a smaller and more uniform deformation.

### 3.2. Schmid factor simulations of rock salt crystals with 100 coating texture

As mentioned above, the possible slip systems for the rock salt structures are  $\{100\} \langle 110 \rangle$ ,  $\{110\} \langle 110 \rangle$  and  $\{111\} \langle 110 \rangle$ . For the

$\{100\} \langle 110 \rangle$  type slip systems, each slip plane (one of the three  $\{100\}$ ) contains two slip directions belonging to  $\langle 110 \rangle$ , as shown in Fig. 4 (a), and there are thus six slip systems in total. For the  $\{110\} \langle 110 \rangle$  slip systems, each slip plane (one of the six  $\{110\}$ ) contains one slip direction, as shown in Fig. 4 (b), and there are six slip systems in total. Fig. 4 (c) shows the third possible type of slip systems,  $\{111\} \langle 110 \rangle$ , which is common for face centered cubic (FCC) metals. For these slip systems, each slip plane (one of the four  $\{111\}$ ) contains three slip directions, as shown in Fig. 4 (c), and there are twelve slip systems in total.

The simulation of Schmid factors for textured rock salt coatings consider the effect on all slip systems for each type (six for  $\{100\} \langle 110 \rangle$  and  $\{110\} \langle 110 \rangle$ , and twelve for  $\{111\} \langle 110 \rangle$ ) upon the loading orientation of the external force. The Schmid factor ( $m$ ) for each slip system is calculated according to [42]:

$$m = \cos\phi \cdot \cos\lambda \quad (1)$$

where  $\phi$  is the angle between the loading direction and the slip direction, and  $\lambda$  is the angle between the loading direction and the normal direction of the slip plane, in the crystal coordinate system.

The loading angle of the resulting external force ( $F$ ) is defined in the specimen coordinate, as shown in Fig. 4 (d). Considering the random in-plane rotation (around the coating normal direction) of the textured grains, it is easier to define the loading force angle by a polar angle ( $\theta$ ) and an azimuthal angle ( $\varphi$ ) in a spherical coordinate system (specimen coordinates). The polar angle ( $\theta$ ) is the angle between the loading force and the coating normal direction (the Z direction), ranging from  $0^\circ$  to  $90^\circ$ , and the azimuthal angle ( $\varphi$ ) is the in-plane rotation angle (within the X-Y plane), rotating anti-clockwise from the X direction, ranging from  $0^\circ$  to  $360^\circ$ . To calculate the Schmid factors for a certain grain in the coating, one needs to correlate the crystal orientation of the grain in the specimen coordinate system. This is usually done by introducing three Euler angles or a matrix describing the relative rotation between the crystal coordinate system and the specimen coordinate system.

For a 100 orientated grain, we define the  $[001]$  direction in the crystal frame is aligned with the Z direction (the coating normal direction) in the specimen frame. For convenience, the  $[010]$  crystal direction is aligned with the Y direction in the specimen coordinate system, and the  $[100]$  crystal direction is aligned with the X direction in the specimen coordinate system. Therefore, the angles  $\phi$  and  $\lambda$  in the crystal coordinate system are thus correlated to the polar ( $\theta$ ) and azimuthal ( $\varphi$ ) angles in the specimen coordinate system, and the Schmid factor ( $m$ ) can be defined as a function of the polar ( $\theta$ ) and the azimuthal ( $\varphi$ ) angles.

First we use the  $\{100\} \langle 110 \rangle$  slip systems for the rock salt structure to demonstrate the Schmid factor diagrams. Fig. 4 (e) and (f) show the Schmid factor diagrams of the  $(001)\bar{1}10$  and  $(001)110$  slip systems for a grain with a 100 orientation (along the coating normal direction). As defined by Shoja et al. [9], the Schmid factor diagram presents a four-dimensional (4D) dataset, including the loading angle of the resulting force (in three-dimensions (3D)) and the corresponding Schmid factor value ( $m$ ) at each loading angle. The polar angle ( $\theta$ ) and the azimuthal ( $\varphi$ ) angle are presented in a stereographic projection, as shown in Fig. 4 (e) and (f). The polar angle ( $\theta$ ) increases longitudinally from the diagram center ( $0^\circ$ ) to the edge ( $90^\circ$ ). The azimuthal angle ( $\varphi$ ) increases from  $0^\circ$  (aligned with the X direction) to  $360^\circ$  anti-clockwise. The dashed circles with arrows (anti-clockwise) in the diagrams (Fig. 4 (e) and (f)) indicate the variation of the azimuthal angle ( $\varphi$ ) changing from  $0^\circ$  to  $360^\circ$ , while keeping the polar angle ( $\theta$ ) at  $45^\circ$ . The dashed lines with arrows (pointing from Z to X) indicate the variation of the polar angle ( $\theta$ ) from  $0^\circ$  to  $90^\circ$ , while keeping the azimuthal angle ( $\varphi$ ) at  $0^\circ$ .

As proposed in reference [9], only the absolute values of the Schmid factors are shown, because dislocation movement is allowed in both a given slip direction and its opposite direction [43]. Fig. 4 (g) shows the Schmid factor as a function of azimuthal angle ( $\varphi$ : from  $0^\circ$  to  $360^\circ$ , while keeping  $\theta$  at  $45^\circ$ ) along the dashed arrow circles in Fig. 4 (e) (red) and (f) (blue), respectively. Fig. 4 (h) shows the Schmid factor as a function of



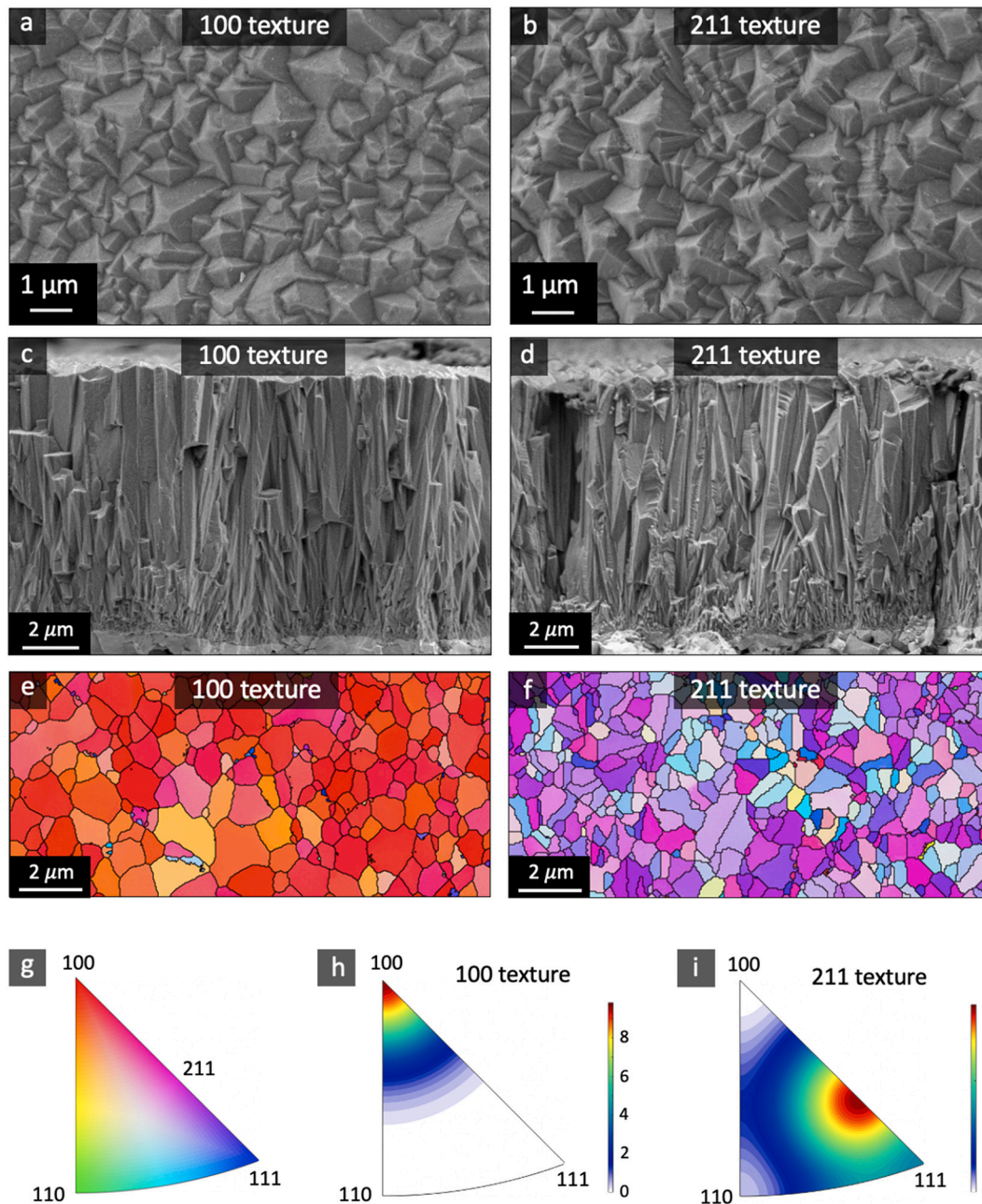


**Fig. 2.** Texture analysis of the Ti(C,N) coatings. (a) and (b) Plan view SEM micrographs of the Ti(C,N) coatings with 100 and 211 textures, respectively. (c) and (d) Fracture cross sectional SEM micrographs of the Ti(C,N) coatings with 100 and 211 textures, respectively. (e) and (f) EBSD IPF maps along the coating normal direction (out of plane), obtained from plan view sections of the 100 and 211 textured Ti(C,N) coatings, respectively. (g) Colour legend of crystallographic orientations in the IPF maps. (h) IPF of the 100 textured coating. (i) IPF of the 211 textured coating.

polar angle ( $\theta$ : from  $0^\circ$  to  $90^\circ$ , while keeping  $\varphi$  at  $0^\circ$ ) along the dashed arrow lines in Fig. 4 (e) and (f) (with identical values in black). The maximum (absolute) value of the Schmid factor is 0.5, which means the dislocation slip is most easily activated for the corresponding loading direction. The minimum (absolute) value of the Schmid factor is 0, which means that dislocation slip cannot happen for the corresponding loading direction.

The Schmid factor diagrams for all six slip systems of the  $\{100\}<110>$  (including  $(001)[\bar{1}10]$ ,  $(010)[10\bar{1}]$ ,  $(100)[01\bar{1}]$ ,  $(001)[110]$ ,  $(010)[101]$  and  $(100)[011]$ ) are calculated and shown in Fig. 5 (a). For each loading orientation, the ability of plastic deformation is influenced by the Schmid factor values for all six slip systems. Therefore, a complete Schmid factor diagram is calculated by superimposing the diagrams of

all slip systems, where for each loading orientation the maximum Schmid factor is chosen from the corresponding values of all slip systems. The complete Schmid diagram simulated for the 100 orientated grain with  $\{100\}<110>$  slip systems and varying force angles is shown in Fig. 5 (b).

Following the same principle, Schmid factor diagrams of all six slip systems of the  $\{110\}<110>$  type (including  $(110)[\bar{1}10]$ ,  $(\bar{1}10)[110]$ ,  $(011)[0\bar{1}1]$ ,  $(01\bar{1})[011]$ ,  $(101)[10\bar{1}]$  and  $(10\bar{1})[101]$ ) were calculated, and are shown in Fig. 6 (a). A corresponding complete Schmid diagram was obtained by imposing the maximum Schmid factor values of these six diagrams, as shown in Fig. 6 (b).

Fig. 7 (a) shows the Schmid factor diagrams of all 12 slip systems of the  $\{111\}<110>$  type (including  $(\bar{1}\bar{1}1)[101]$ ,  $(\bar{1}\bar{1}1)[\bar{1}01]$ ,  $(1\bar{1}\bar{1})[101]$ ,

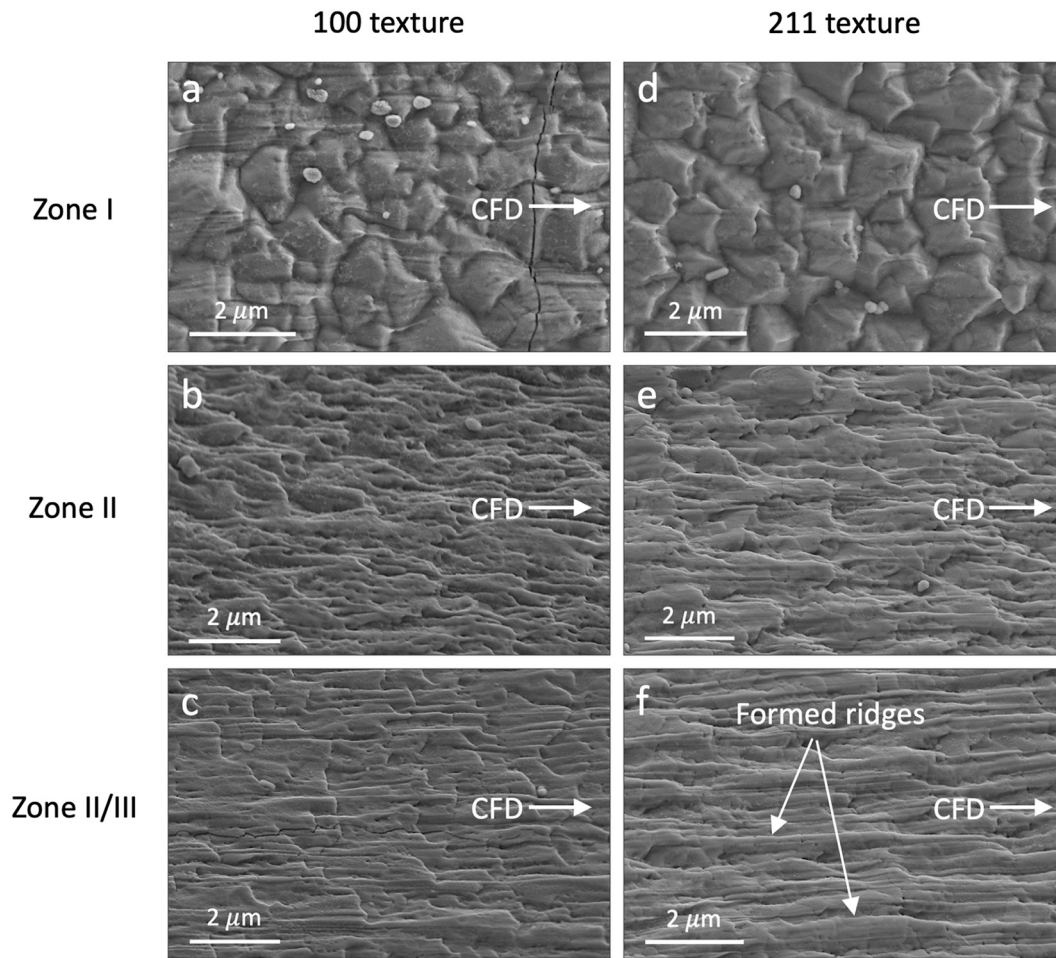


**Fig. 3.** SEM micrographs of the Ti(C,N) coatings on the worn rake face of the cutting tool inserts. (a), (b) and (c) the 100 textured coating in zone I, II and II/III, respectively. (d), (e), and (f) micrographs of the 211 textured coating in zone I, II and II/III, respectively. The chip flow direction (CFD) is indicated by arrows. Ridges formed due to large plastic deformation in (f) are marked.

(111)[ $\bar{1}01$ ], ( $\bar{1}\bar{1}1$ )[011], ( $\bar{1}\bar{1}\bar{1}$ )[011], ( $\bar{1}\bar{1}\bar{1}$ )[ $0\bar{1}1$ ], (111)[ $0\bar{1}1$ ], ( $\bar{1}\bar{1}1$ )[ $1\bar{1}0$ ], ( $\bar{1}\bar{1}\bar{1}$ )[110], ( $\bar{1}\bar{1}\bar{1}$ )[110], and (111)[ $1\bar{1}0$ ]]. A corresponding complete Schmid diagram was obtained by imposing the maximum Schmid factor values of these twelve diagrams, as shown in Fig. 7 (b).

### 3.3. Schmid factor simulation of rock salt crystals with 211 coating textures

As mentioned above, the diagrams shown in Figs. 5 (b), 6 (b) and 7 (b) present the Schmid factors of a rock salt crystal with a 100 orientation. Different orientations of the crystal would influence the activation of its slip systems with respect to the external force, and thus cause different Schmid factor diagrams. Here, we now calculate Schmid factor diagrams for rock salt structures with 211 orientation (along the coating normal, i.e. 211 texture), and compare with the results of the 100 orientation.

Following the same principle as above for the 100 grain orientation, now aligning the [211] direction parallel to the coating normal direction, the complete Schmid factor diagrams of the 211 orientated grains are obtained. Fig. 8 shows the corresponding diagrams for the {100}<110> (Fig. 8 (a)), {110}<110> (Fig. 8 (b)), and {111}<110> (Fig. 8 (c)) slip systems.

The symmetries of the Schmid factor diagrams are given by the symmetries of the rock salt crystal structure. For the 100 oriented crystal, the Schmid factor diagrams exhibit a four-fold rotational symmetry, see Figs. 5 (b), 6 (b) and 7 (b), which coincides with the rotational

symmetry around the <100> directions of the rock salt crystal. However, the Schmid factor diagrams for the 211 oriented crystal have no rotational symmetry around the coating normal, as shown in Fig. 8.

### 3.4. Schmid factors of polycrystalline coatings with rock salt structure

Schmid factor analysis for fibre-textured coatings is developed based on the Schmid factor diagrams calculated for the ideally orientated crystals in Figs. 5 (b), 6 (b), 7 (b) and 8. It is assumed that the coating grains exhibit a random rotation around the coating normal, while maintaining their orientation (texture) along the coating normal. Thus, for each polar angle ( $\theta$ ), the average Schmid factor (over all grains within the coating) is deduced from all azimuthal angles ( $\varphi$ ). The averaged Schmid factor value ( $\bar{m}$ ) as a function of the polar angle ( $\theta$ ) is calculated for ideally textured coatings, see Figs. 9, 10 and 11. The error bar is defined as the standard deviation of all Schmid factor values at different azimuthal angles ( $\varphi$ ) for a certain polar angle ( $\theta$ ).

Fig. 9 shows the Schmid factor results for the {100}<110> slip system. As shown in Fig. 9 (a), for the 100 textured coating, the averaged Schmid factor ( $\bar{m}$ ) has a minimum value at low polar angle  $\theta$  (around the center of the diagram shown in Fig. 5 (b)), and increases with higher polar angle and reaches a maximum average value at  $\theta = 40^\circ$ . As mentioned above, the polar angle of the resulting force for zone I is around  $10^\circ$ , while at zone II/III it is around  $45^\circ$ . The corresponding  $\bar{m}$  values are indicated in Fig. 9 (a):  $\bar{m} = 0.16$  for  $10^\circ$ ;  $\bar{m} = 0.45$  for  $45^\circ$ . For the 211 textured coating, the averaged Schmid factor has a maximum

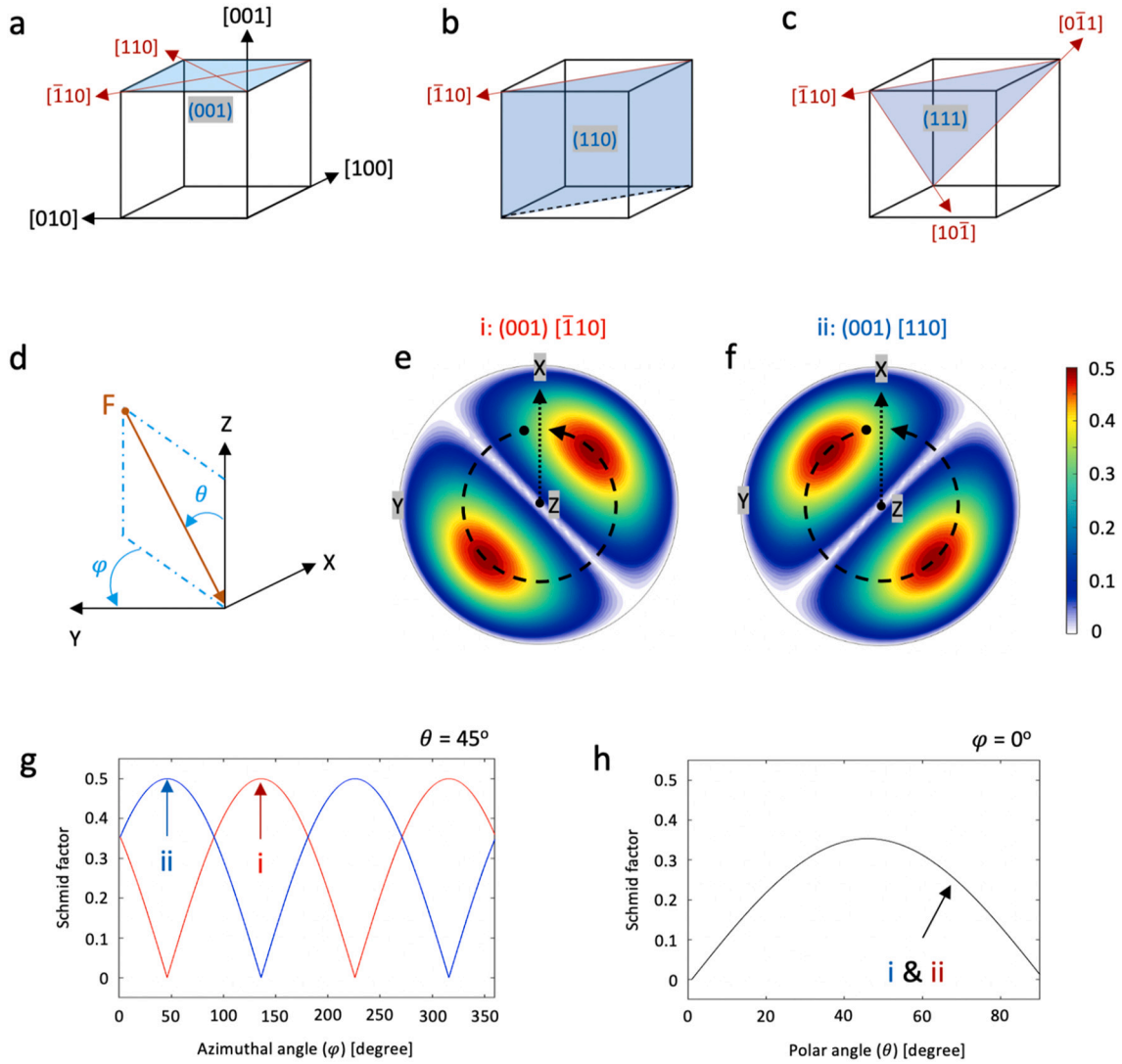


**Fig. 4.** Schematic of Schmid factor calculations. (a), (b) and (c) Illustration of the three types of slip systems for rock salt structured materials:  $\{100\} \langle 110 \rangle$ ,  $\{110\} \langle 110 \rangle$ , and  $\{111\} \langle 110 \rangle$ , respectively. (d) Schematic of the resulting external force ( $F$ ) direction during the metal machining process in the specimen coordinate system. The polar ( $\theta$ ) and the azimuthal ( $\varphi$ ) angles used to define the loading direction in a spherical coordinate system of the specimen frame. (e) and (f) Simulated Schmid factor diagrams for the  $(001)[\bar{1}10]$  and  $(001)[110]$  slip systems for the rock salt grain with 100 growth orientation, respectively. The diagrams are presented using stereographic projection, where the specimen coordinates ( $X$ ,  $Y$  and  $Z$ ) are indicated. The dashed circles with arrows (anti-clockwise) indicate the variation of the azimuthal angle ( $\varphi$ ) changing from  $0^\circ$  to  $360^\circ$ , while keeping the polar angle ( $\theta$ ) at  $45^\circ$ . The dotted lines with arrows (pointing from  $Z$  to  $X$ ) indicate the variation of the polar angle ( $\theta$ ) from  $0^\circ$  to  $90^\circ$ , while keeping the azimuthal angle ( $\varphi$ ) at  $0^\circ$ . (g) Schmid factors as a function of azimuthal angle ( $\varphi$ : from  $0^\circ$  to  $360^\circ$ ), while keeping  $\theta$  at  $45^\circ$  along the dashed arrow circles in (e) (blue) and (f) (red), respectively. (h) Schmid factors as a function of polar angle ( $\theta$ : from  $0^\circ$  to  $90^\circ$ ), while keeping  $\varphi$  at  $0^\circ$  along the dashed arrow lines in (e) and (f) (identical, black colour). (For interpretation of the references to colour in this figure legend, the reader is referred to the web version of this article.)

value at low polar angle, decreases with higher polar angles and reaches a stable plateau from around  $\theta = 23^\circ$ , see Fig. 9 (b):  $\bar{m} = 0.45$  for  $10^\circ$ ;  $\bar{m} = 0.37$  for  $45^\circ$ . It worth noting that there is a large spread of  $\bar{m}$  values at zone II/III ( $45^\circ$ ), reflecting the larger difference between grains with different azimuthal angles.

Fig. 10 shows the  $\bar{m}$  value as a function of polar angle ( $\theta$ ) for textured coatings with the  $\{110\} \langle 110 \rangle$  as active slip systems. For the 100 textured coating, the averaged Schmid factor has a maximum value at low polar angle (zone I), and decreases with higher polar angle, where the minimum value of  $\bar{m}$  appears close to  $45^\circ$ , see Fig. 10 (a):  $\bar{m} = 0.48$  for  $10^\circ$ ;  $\bar{m} = 0.21$  for  $45^\circ$ . Fig. 10 (b) shows the variation of  $\bar{m}$  value for a 211 textured coating. The  $\bar{m}$  values lie in a region between 0.25 and 0.35 for all polar angles. The  $\bar{m}$  is around 0.28 for zone I ( $\theta = 10^\circ$ ) and 0.35 for zone II/III ( $\theta = 45^\circ$ ).

The averaged Schmid factor  $\bar{m}$  as a function of loading polar angle ( $\theta$ )

for the  $\{111\} \langle 110 \rangle$  slip system is presented in Fig. 11. In general, the  $\bar{m}$  values are higher for both the 100 and 211 textures for these slip systems. This is because the  $\{111\} \langle 110 \rangle$  contains more slip systems (twelve instead of six) and this makes the complete Schmid factor diagrams more isotropic (and with higher values in general, see Fig. 8 (c)) than that of  $\{100\} \langle 110 \rangle$  (Fig. 8 (a)) and  $\{110\} \langle 110 \rangle$  (Fig. 8 (b)). For the 100 and 211 textured coatings, the  $\bar{m}$  values lie in a range between 0.4 and 0.5, and are not much influenced by the polar angle ( $\theta$ ), see Fig. 11. The corresponding  $\bar{m}$  values for zone I and zone II/III are labelled for both the 100 and 211 textures in Fig. 11. The similar  $\bar{m}$  values for both textures and wear zones indicate that the ability for plastic deformation is quite independent of texture and external force angle for these slip systems.

When a fibre textured coating is loaded by a resulting force with a certain inclination/polar angle ( $\theta$ ), grains will have different Schmid



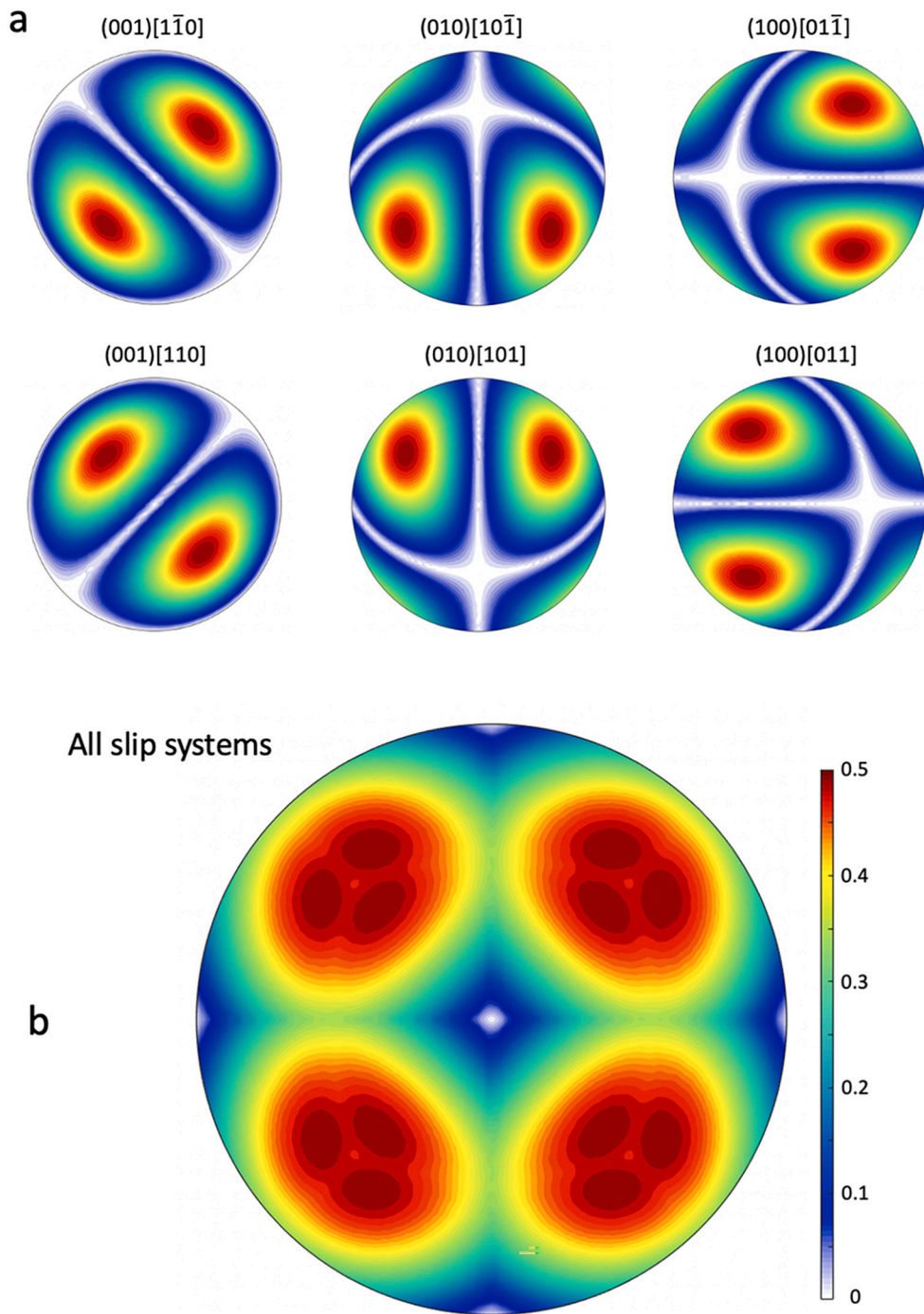


**Fig. 5.** Schmid factor diagrams calculated for the  $\{100\}\langle 110 \rangle$  slip systems of the 100 orientated grain. (a) Schmid factor diagrams of the six slip systems belonging to  $\{100\}\langle 110 \rangle$ . (b) Schmid factor diagram obtained by combining the local maximum values of the six diagrams in (a).

factors (the origin of the spread in Figs. 9, 10 and 11), because they are randomly rotated around the coating normal direction, resulting in different azimuthal angles ( $\varphi$ ) relative to the loading force. This means that in a given wear zone, grains will have different  $m$  values for the same slip system, leading to different degrees of plastic deformation (for that slip system). Figs. 12 and 13 show the spread of simulated Schmid factors in zones I and II/III, for different slip systems and textures. Due to the spread of grain growth directions along the coating normal, i.e., the coating fibre texture is not perfect,  $m$  values within a window of  $\pm 5^\circ$  centered around the ideal polar angle ( $10^\circ$  for zone I, and  $45^\circ$  for zone II/III) were considered. This corresponds to a variation of external force with  $\pm 5^\circ$  polar angle for a perfect fibre texture. For zone I, the  $m$  values

corresponding to polar angles within a range of  $10 \pm 5^\circ$  are presented, see Fig. 12. For zone II/III, the  $m$  values corresponding to polar angles within a range of  $45 \pm 5^\circ$  are presented, see Fig. 13.

#### 4. Discussion

##### 4.1. Influence of texture and polar angle on Schmid factors

According to the simulated Schmid factor diagrams, the  $\{111\}\langle 110 \rangle$  slip systems show higher  $m$  values with lower spread (Figs. 7 (b) and 8 (c)) than those for the  $\{100\}\langle 110 \rangle$  (Figs. 5 (b) and 8 (a)) and  $\{110\}\langle 110 \rangle$  systems (Figs. 6 (b) and 8 (b)). This is also reflected by the



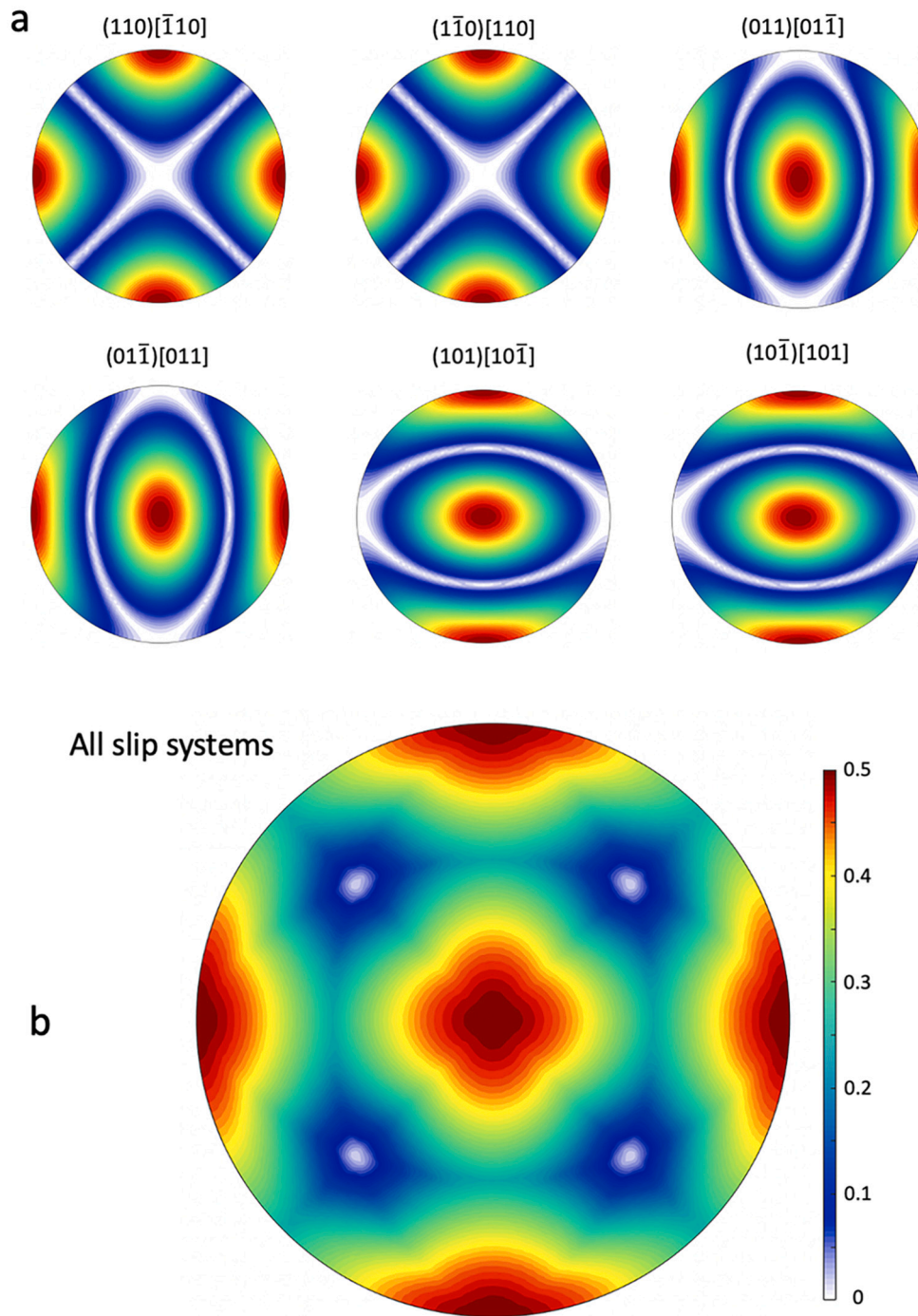


**Fig. 6.** Schmid factor diagrams calculated for the  $\{110\}\langle 110\rangle$  slip systems of the 100 orientated grain. (a) Schmid factor diagrams of the six slip systems belonging to  $\{110\}\langle 110\rangle$ . (b) Schmid factor diagram obtained by combining the local maximum values of the six diagrams in (a).

higher averaged Schmid factor values ( $\bar{m}$ ) with smaller error bars in the  $\bar{m} - \theta$  plots of the  $\{111\}\langle 110\rangle$  systems (Fig. 11) than those of the  $\{100\}\langle 110\rangle$  (Fig. 9) and the  $\{110\}\langle 110\rangle$  (Fig. 10) systems. The frequency diagrams also reveal that the  $\{111\}\langle 110\rangle$  systems have a lower spread of the  $m$  values (but with higher values close to 0.5) in both zone I (Fig. 12) and zone II/III (Fig. 13) for different textures, compared to the other two types of the slip systems. This low spread of  $m$  values (with high values close to 0.5) for the  $\{111\}\langle 110\rangle$  is due to that the  $\{111\}\langle 110\rangle$  contains more (twelve) equivalent slip systems that could respond to the external force, compared to the  $\{100\}\langle 110\rangle$  and  $\{110\}\langle 110\rangle$  systems (six in each case). In addition, it is obvious that, for the  $\{111\}\langle 110\rangle$  slip systems, the coating fibre texture and the external force polar

angle ( $\theta$ ) have negligible influence on the averaged Schmid factor values ( $\bar{m}$ ) and the spread of the  $m$  values, see Figs. 11, 12 and 13.

In comparison, when the activated slip systems are either  $\{100\}\langle 110\rangle$  or  $\{110\}\langle 110\rangle$ , the coating texture and the polar angle ( $\theta$ ) of the external force have more influence on the average and spread of the Schmid factor values than that of  $\{111\}\langle 110\rangle$ . The overall averaged Schmid factor values ( $\bar{m}$ ) for the  $\{100\}\langle 110\rangle$  and  $\{110\}\langle 110\rangle$  slip systems are lower compared to the  $\{111\}\langle 110\rangle$ , for most polar angles and different textures (Figs. 9, 10 and 11). This is due to the fewer slip combinations in these two types of slip systems.

For the  $\{100\}\langle 110\rangle$  slip systems, in zone I, the  $m$  values spread between 0.07 and 0.25 for the 100 texture (Fig. 12), and spread between

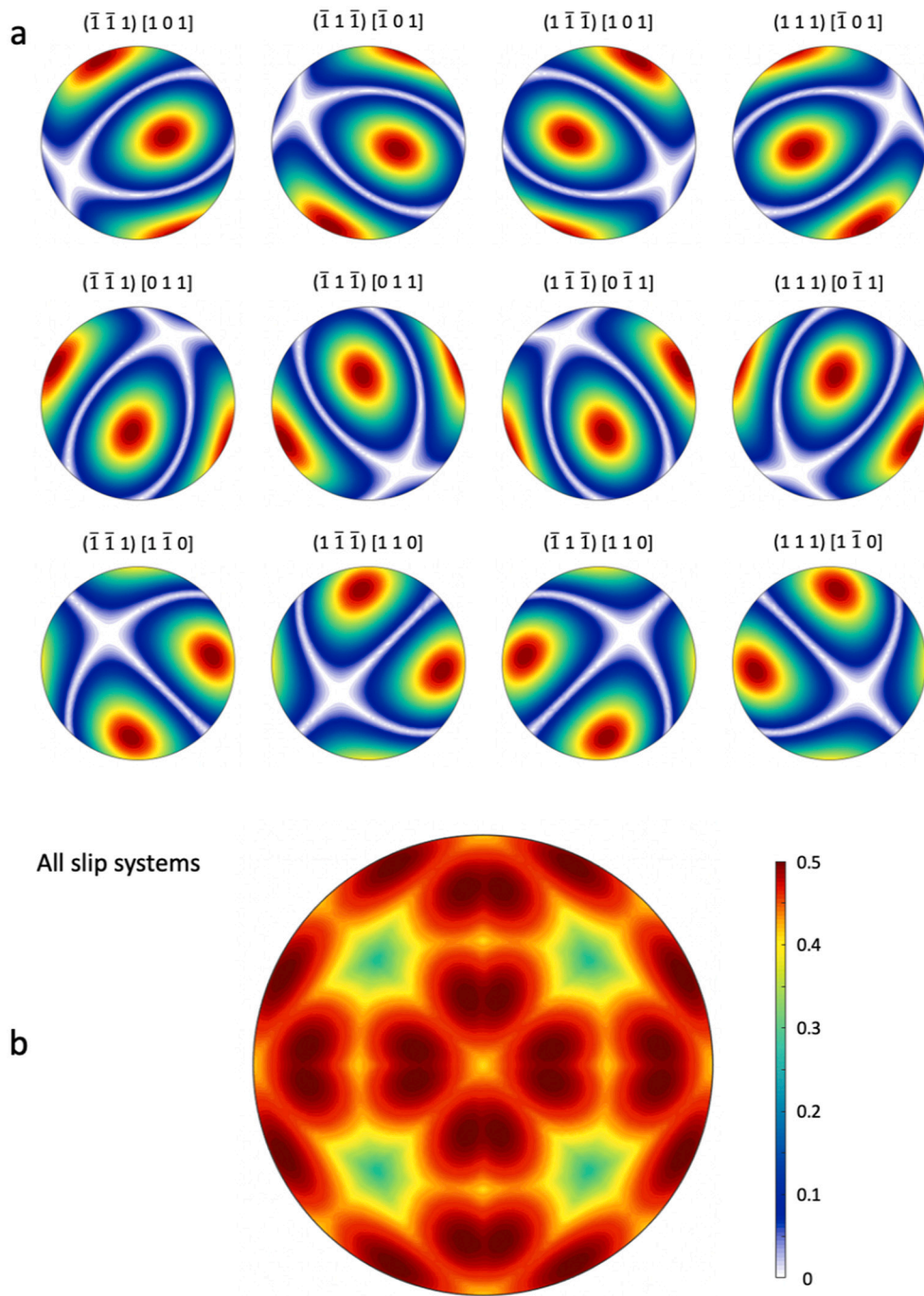


**Fig. 7.** Schmid factor diagrams calculated for the  $\{111\}\langle 110 \rangle$  slip systems of the 100 orientated grain. (a) Schmid factor diagrams of the twelve slip systems belonging to  $\{111\}\langle 110 \rangle$ . (b) Schmid factor diagram obtained by combining the local maximum values of the twelve diagrams in (a).

0.32 and 0.5 for the 211 texture (Fig. 13). Thus, in zone I, the averaged Schmid factor value ( $\bar{m}$ ) is lower for the 100 texture than that for 211 texture (Fig. 9). In the zone II/III,  $m$  values spread between 0.35 and 0.5 for the 100 texture (Fig. 12), and spread between 0.1 and 0.5 for the 211 texture (Fig. 13). Thus, in the zone II/III, the averaged Schmid factor value ( $\bar{m}$ ) is higher for the 100 texture than that for 211 texture (Fig. 9).

For the  $\{110\}\langle 110 \rangle$  slip systems, in zone I, the  $m$  values spread between 0.45 and 0.5 for the 100 texture (Fig. 12), and spread between 0.06 and 0.42 for the 211 texture (Fig. 13). Thus, in zone I, the averaged Schmid factor value ( $\bar{m}$ ) is higher for the 100 texture than that for 211 texture (Fig. 10). In the zone II/III,  $m$  values spread between 0.05 and 0.3 for the 100 texture (Fig. 12), and spread between 0.15 and 0.5 for the

211 texture (Fig. 13). Thus, in the zone II/III, the averaged Schmid factor value ( $\bar{m}$ ) is higher for the 211 texture than that for 100 texture (Fig. 10).

#### 4.2. Influence of texture and slip systems on the coating plastic deformation

The amount of plastic deformation of the Ti(C,N) coating depends on several factors, including the  $m$  values of grains, the applied stress during the metal machining process, and the (temperature dependent) critical resolved shear stress (CRSS) of the slip system. As has been explored in this work, the  $m$  values depend on the fibre texture that remains invariant with location, and the local loading direction of the

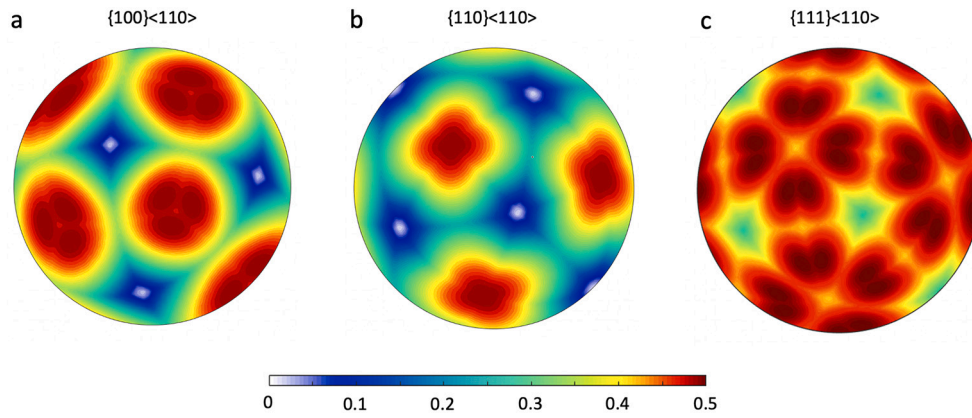


Fig. 8. Schmid factor diagrams of the (a)  $\{100\}<110>$ , (b)  $\{110\}<110>$  and (c)  $\{111\}<110>$  slip systems, respectively, for a crystal with a 211 orientation.

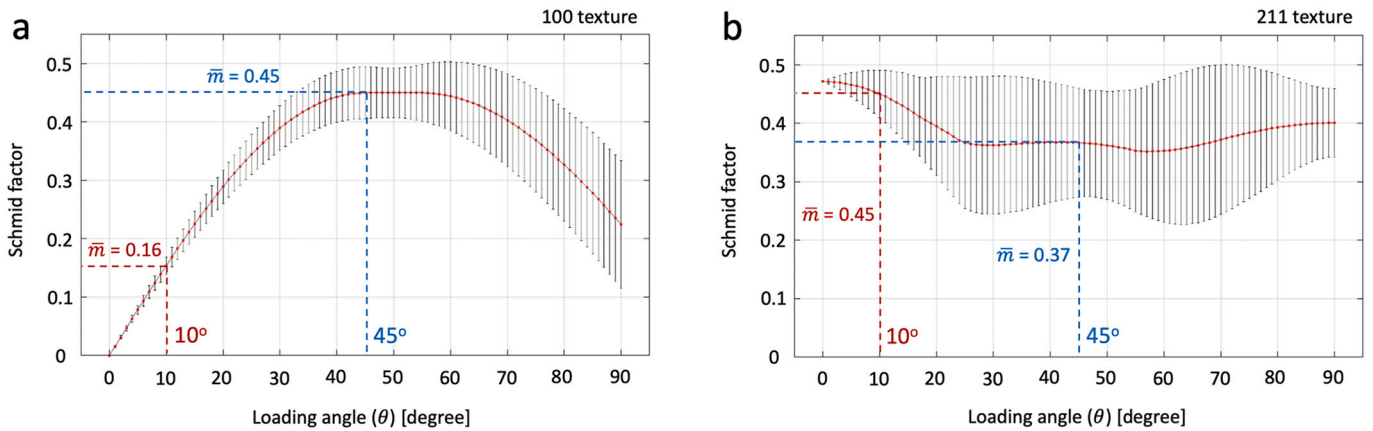


Fig. 9. Averaged Schmid factor ( $\bar{m}$ ) as a function of external force polar angle ( $\theta$ ) calculated for the  $\{100\}<110>$  slip systems of coatings with ideal (a) 100 and (b) 211 textures, respectively. The spread for the Schmid factor value at each polar angle ( $\theta$ ) represents the standard deviation of the values from all azimuthal angles ( $\varphi$ ) from  $0^\circ$  to  $360^\circ$ .

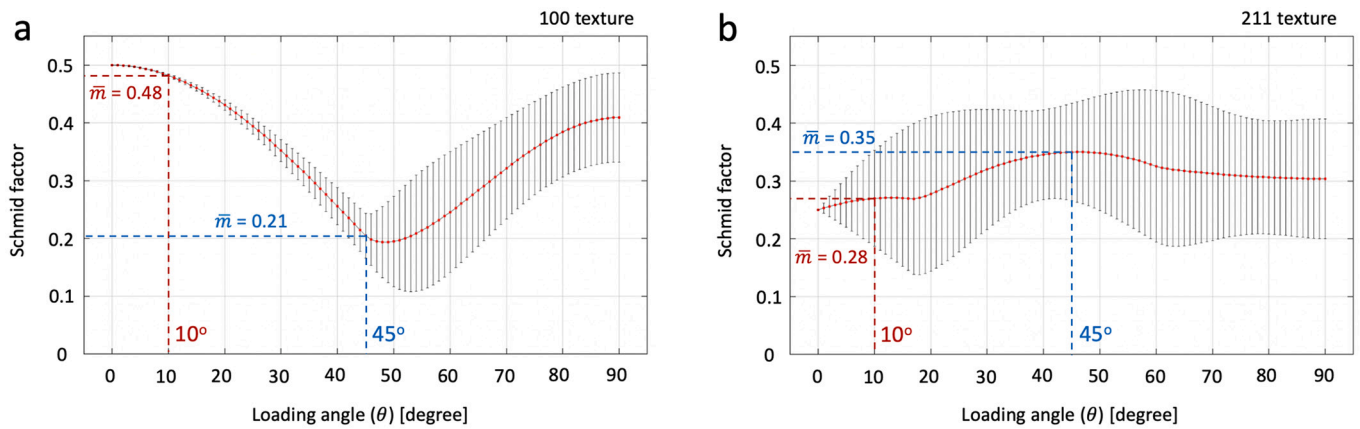


Fig. 10. Averaged Schmid factor ( $\bar{m}$ ) as a function of external force polar angle ( $\theta$ ) calculated for the  $\{110\}<110>$  slip systems of coatings with ideal (a) 100 and (b) 211 textures, respectively. The spread for the Schmid factor value at each polar angle ( $\theta$ ) represents the standard deviation of the values from all azimuthal angles ( $\varphi$ ) from  $0^\circ$  to  $360^\circ$ .

external force that varies in different wear zones. The applied stress, including the magnitude and loading direction, changes with location on the cutting tool insert [7]. The CRSS depends on the activation of different slip systems, and is thus influenced by the local temperature, which also changes with location on the cutting tool insert [7].

To study the influence of fibre texture on the plastic deformation of the Ti(C,N) coatings, the same wear zones (same location) on the 100

and 211 textured samples need to be compared, because all other influencing factors vary between different zones. In addition, the activated slip systems in each zone could be evaluated according to the observed difference of plastic deformation between the 100 and 211 textured coatings.

As discussed in Section 4.1, the  $\{111\}<110>$  slip systems have  $m$  with high values spreading within a narrow span close to 0.5 for



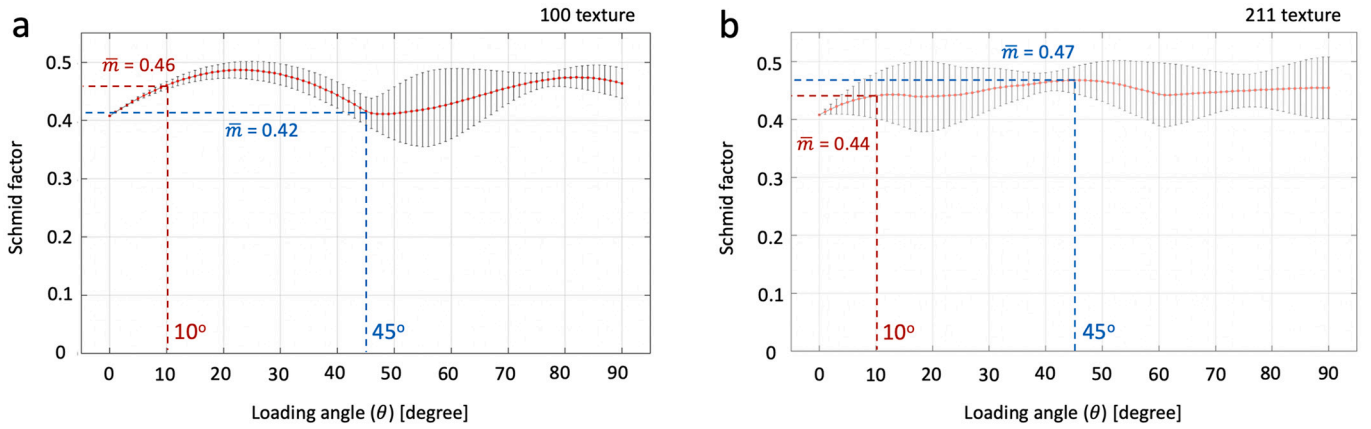


Fig. 11. Averaged Schmid factor ( $\bar{m}$ ) as a function of the external force polar angle ( $\theta$ ) calculated for the  $\{111\}\langle 110\rangle$  slip systems of coatings with ideal (a) 100 and (b) 211 textures, respectively. The spread of the Schmid factor value at each polar angle ( $\theta$ ) represents the standard deviation of the values from all azimuthal angles ( $\varphi$ ) from  $0^\circ$  to  $360^\circ$ .

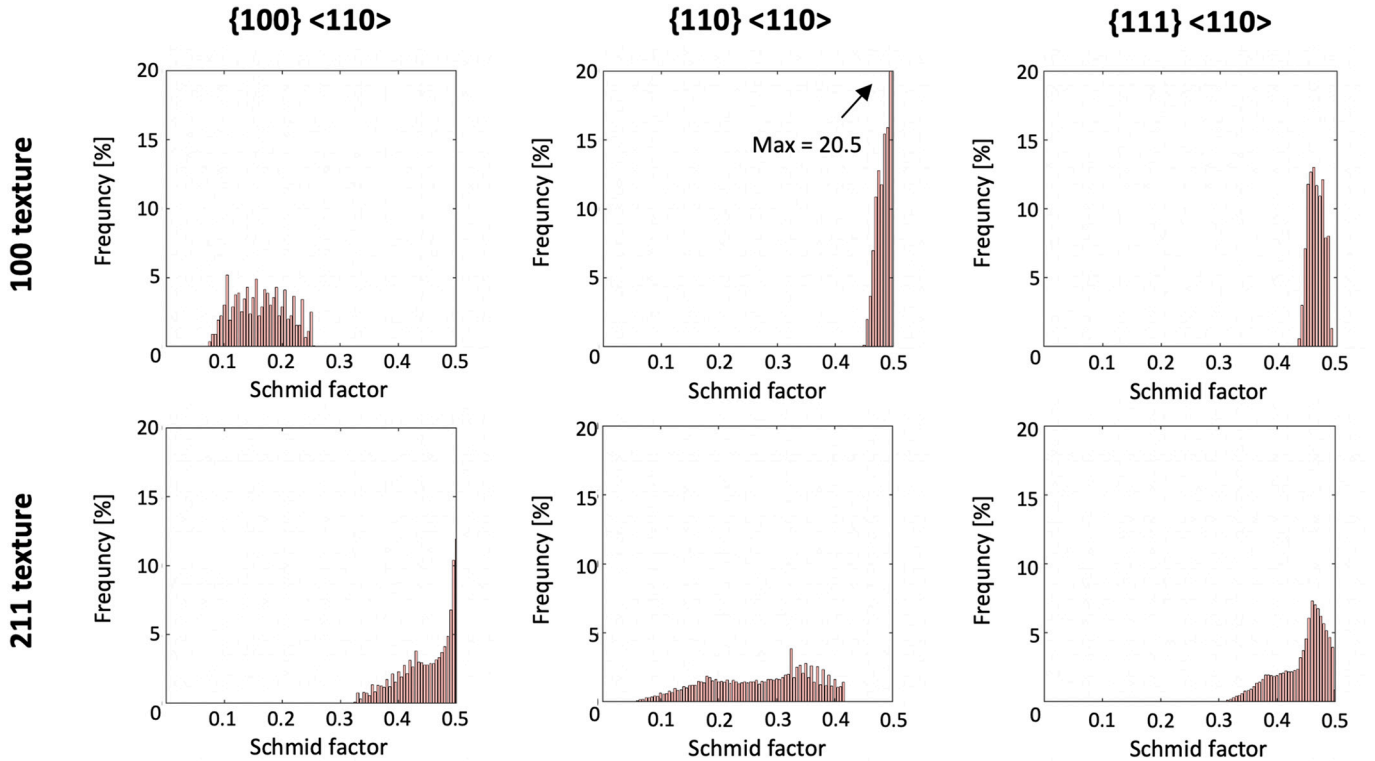


Fig. 12. Frequency diagrams for the simulated Schmid factors of different slip systems and textures, for an external force polar angle of  $10^\circ \pm 5^\circ$ , corresponding to zone I.

different textures and wear zones. This means that when it comes to machining operations, for the rock salt structured polycrystalline coatings that have the  $\{111\}\langle 110\rangle$  slip systems activated, the fibre texture and the polar angle of the external force have no significant influence on the degree of plastic deformation of the coatings. In addition, due to the low spread of the  $m$  values for the  $\{111\}\langle 110\rangle$ , the plastic deformation is expected to be isotropic for the different textures and polar angles. The same principle can be applied to polycrystalline FCC metallic materials with  $\{111\}\langle 110\rangle$  as the activated slip systems.

However, as shown in see Fig. 3, the degree of plastic deformation of the Ti(C,N) coatings was found to vary with both the coating texture and the external force polar angle (wear zone). It indicates that the (dominant) activated slip systems under the corresponding condition of the

machining process (e.g. the thermal and pressure loads) are not  $\{111\}\langle 110\rangle$ .

In zone I, more plastic deformation was found for the 100 textured coatings than for the 211 textured coatings. In zone II/III, more plastic deformation was found for the 211 textured coatings than for the 100 textured coatings. These observations imply that the  $m$  values are higher for the 100 texture than the 211 texture at low polar angles ( $\theta = 10^\circ$  for zone I), and are higher for the 211 texture than the 100 texture at high polar angles ( $\theta = 45^\circ$  for zone II/III). According to the analysis in Section 4.1, this suggests that the dominant activated slip systems for the Ti(C,N) coatings under the condition of the metal machining process in this work are  $\{110\}\langle 110\rangle$ .

In addition, the 211 textured coating exhibits a more anisotropic

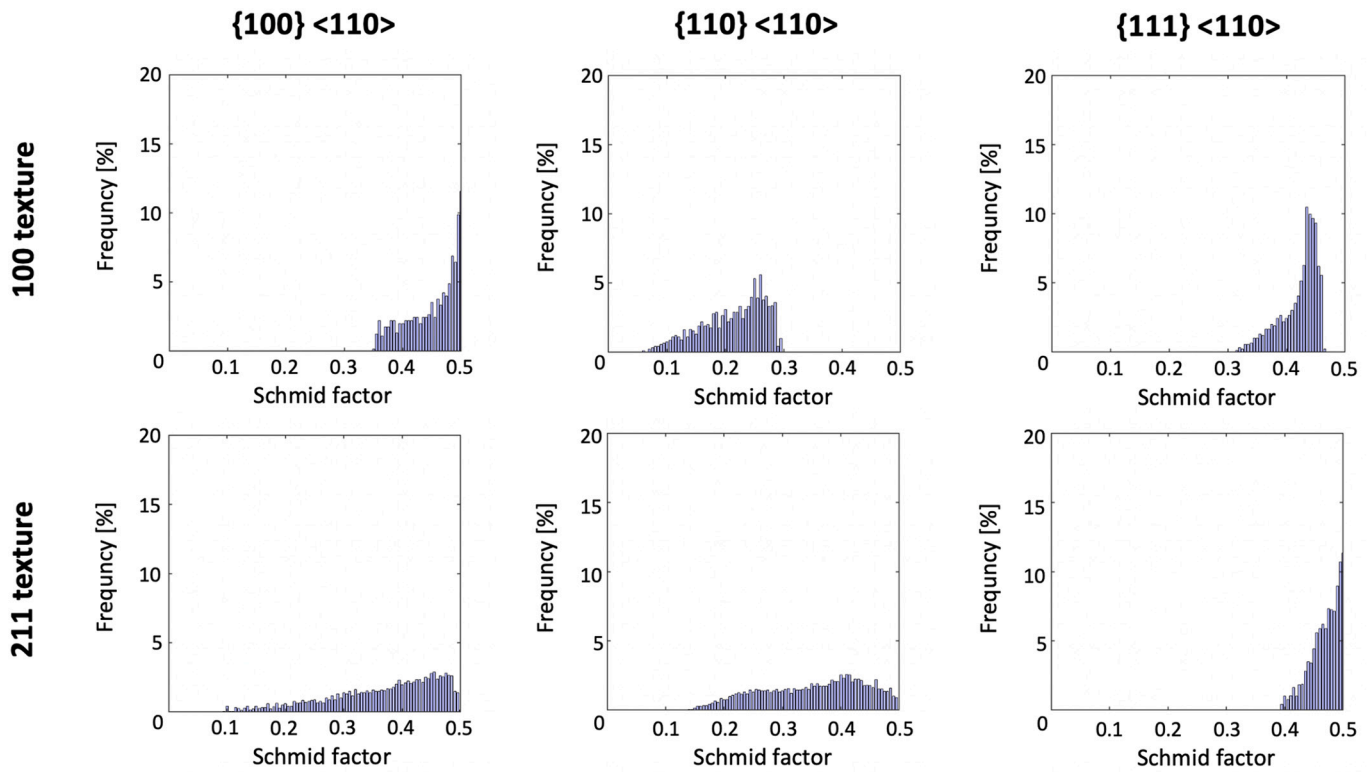


Fig. 13. Frequency diagrams for the simulated Schmid factors of different slip systems and textures, for an external force polar angle of  $45^\circ \pm 5^\circ$ , corresponding to zone II/III.

deformation for the Ti(C,N) grains, where some grains deformed more heavily than others, creating long ridges in zone II/III (see Fig. 3 (f)). This could be due to that these grains have  $m$  values spreading in a wide range for the  $\{110\}\langle 110 \rangle$  (see Fig. 13), and some of them with high  $m$  values (close to the 0.5) were more elongated. However, the grains in the 100 textured coating, having lower  $m$  values spreading in a narrower range for the  $\{110\}\langle 110 \rangle$  (see Fig. 13), shows less deformation and a more isotropic response for the Ti(C,N) grains.

#### 4.3. Considerations of the activated slip systems

Although the slip systems of Ti(C,N) have not been reported, the slip systems of other cubic metal carbides and nitrides, such as titanium carbide (TiC [36,37,44,45]) and titanium nitride (TiN [31,46]), have been studied and can serve as starting points for understanding the plastic deformation of Ti(C,N). Using density functional theory (DFT) simulations, Yadav et al. studied Peierls stress [47] on different slip systems of the TiN, where the minimum and maximum Peierls stresses were found to exist on the  $\{110\}\langle 110 \rangle$  and the  $\{100\}\langle 110 \rangle$  slip systems, respectively, and the second largest Peierls stress is on the  $\{111\}\langle 110 \rangle$  [46]. Further DFT simulations for the stacking fault energy on different atomic planes of the TiN [31] and TiC [44] also support that the  $\{110\}\langle 110 \rangle$  are the preferred slip systems. However, it should be pointed out that the preferred slip systems can vary with temperature. A brittle to ductile transition (BDT) was observed in TiC, below the BDT temperature (around  $800^\circ\text{C}$ ) the  $\{110\}\langle 110 \rangle$  slip systems are preferred, and above the BDT temperature the  $\{111\}\langle 110 \rangle$  slip systems are preferred [36,37].

Although the observed plastic deformation of the Ti(C,N) coatings in zones I and II/III is consistent with the simulation results for the  $\{110\}\langle 110 \rangle$ , it should be noted that the  $\{100\}\langle 110 \rangle$  and  $\{111\}\langle 110 \rangle$  slip systems could also be activated to some degree due to the extreme force applied on the cutting tool surfaces during machining, and the high local temperatures, as reported in [7]. However, it is likely that the local

temperature at the contact between the Ti(C,N) coatings and the workpiece material during the metal machining process is not high enough to generate as large amount of dislocations on the  $\{111\}$  or  $\{100\}$  planes as on the  $\{110\}$  planes. Thus, the  $\{110\}\langle 110 \rangle$  are the dominant slip systems and cause the observed differences in plastic deformation between the 100 and 211 textured coatings.

#### 5. Conclusions

In this work, we have applied a Schmid factor simulation method to analyse the ability of plastic deformation due to the chip flow of wear-resistant coatings with rock salt structure. The simulations were compared to wear on the rake face of two textured Ti(C,N) coatings, tested by longitudinal turning for 1 min. Based on our findings, we come to the following conclusions:

- The 100 textured Ti(C,N) coating shows more plastic deformation in zone I and less plastic deformation in zone II/III than the 211 textured Ti(C,N) coating.
- In the 100 textured coating, grains start to deform plastically in zone II and show a homogeneous deformation in zone II/III. In the 211 textured coating, grains show deformation in zone II and some grains deform more heavily in zone II/III creating long ridges.
- The Schmid factors for the  $\{111\}\langle 110 \rangle$  slip systems are not significantly influenced by the coating texture or by the angle of the resulting cutting force.
- Schmid factors for the  $\{100\}\langle 110 \rangle$  and  $\{110\}\langle 110 \rangle$  slip systems are more dependent on the coating texture and the external force angle.
- The observed surface morphology and grain deformation of the worn coatings of the textured Ti(C,N) coatings on the rake face coincide best with the simulation results of the  $\{110\}\langle 110 \rangle$  slip systems, which are therefore believed to be the dominant activated slip systems during the metal machining tests applied in this work.

This work demonstrates that the plastic deformation behavior during metal machining of wear-resistant coatings with rock salt crystal structure and different growth textures can be understood by Schmid factor simulations. It thus helps to design coatings with desirable wear behavior. In addition, this methodology can be extended to coatings with other crystal structures and growth textures.

### CRedit authorship contribution statement

**Ren Qiu:** Conceptualization, Methodology, Software, Formal analysis, Investigation, Writing – original draft, Visualization. **Siamak Shoja:** Methodology, Validation, Investigation. **Linus von Fieandt:** Resources, Investigation, Writing – review & editing. **Jan Engqvist:** Resources, Investigation, Writing – review & editing. **Olof Bäcke:** Investigation, Supervision, Writing – review & editing, Project administration. **Hans-Olof André:** Writing – review & editing, Supervision. **Mats Halvarsson:** Writing – review & editing, Supervision, Funding acquisition.

### Declaration of Competing Interest

The authors declare that they have no known competing financial interests or personal relationships that could have appeared to influence the work reported in this paper.

### Acknowledgements

Funding from “CVD 2.0”, a Swedish Foundation for Strategic Research program via contract RMA15-0048, is gratefully acknowledged. The microstructural characterizations were mainly carried out at the Chalmers Materials Analysis Laboratory (CMAL).

### References

- [1] H.M. Ortner, P. Ettmayer, H. Kolaska, The history of the technological progress of hardmetals, *Int. J. Refract. Met. Hard Mater.* 44 (2014) 148–159.
- [2] J. García, V. Collado Ciprés, A. Blomqvist, B. Kaplan, Cemented carbide microstructures: a review, *Int. J. Refract. Met. Hard Mater.* 80 (2019) 40–68.
- [3] I. Endler, M. Höhn, M. Herrmann, R. Pitonak, S. Ruppi, M. Schneider, H. van den Berg, H. Westphal, Novel aluminum-rich  $\text{Ti}_{1-x}\text{Al}_x\text{N}$  coatings by LPCVD, *Surf. Coat. Technol.* 203 (2008) 530–533.
- [4] S. Ruppi, Influence of process conditions on the growth and texture of CVD alpha-alumina, *Coatings*. 10 (2020).
- [5] S. Schiller, G. Beister, J. Reschke, G. Hoetzsch, TiN hard coatings deposited on high-speed steel substrates by reactive direct current magnetron sputtering, *J. Vac. Sci. Technol. A Vacuum Surf. Film.* 5 (1987) 2180–2183.
- [6] A. Mani, P. Aubert, H. Khodja, P. Houdy, Mechanical and structural properties of TiC and TiCN thin films grown by RF sputtering, *MRS Online Proc. Libr.* 778 (2004) 613.
- [7] R. M'Saoubi, O. Alm, J.M. Andersson, H. Engström, T. Larsson, M.P. Johansson-Jöesaar, M. Schwind, Microstructure and wear mechanisms of texture-controlled CVD  $\alpha\text{-Al}_2\text{O}_3$  coatings, *Wear*. 376–377 (2017) 1766–1778.
- [8] S. Ruppi, Enhanced performance of  $\alpha\text{-Al}_2\text{O}_3$  coatings by control of crystal orientation, *Surf. Coat. Technol.* 202 (2008) 4257–4269.
- [9] S. Shoja, O. Alm, S. Norgren, H.-O. André, M. Halvarsson, Calculated and experimental Schmid factors for chip flow deformation of textured CVD  $\alpha\text{-alumina}$  coatings, *Surf. Coat. Technol.* 412 (2021), 126991.
- [10] M. Halvarsson, S. Vuorinen, Epitaxy in multilayer coatings of  $\kappa\text{-Al}_2\text{O}_3$ , *Surf. Coat. Technol.* 80 (1996) 80–88.
- [11] S. Ruppi, Deposition, microstructure and properties of texture-controlled CVD  $\alpha\text{-Al}_2\text{O}_3$  coatings, *Int. J. Refract. Met. Hard Mater.* 23 (2005) 306–316.
- [12] R. Qiu, O. Bäcke, D. Stiens, W. Janssen, J. Kümmel, T. Manns, H.-O. André, M. Halvarsson, CVD TiAlN coatings with tunable nanolamella architectures, *Surf. Coat. Technol.* 413 (2021), 127076.
- [13] R. Qiu, A. Forslund, O. Bäcke, A.H.S. Iyer, M. Sattari, W. Janssen, T. Manns, J. Kümmel, A. Ruban, D. Stiens, H.-O. André, M. Halvarsson, Effects of gas flow on detailed microstructure inhomogeneities in LPCVD TiAlN nanolamella coatings, *Materialia*. 9 (2020), 100546.
- [14] R. Qiu, H. Aboulfadl, O. Bäcke, D. Stiens, H.-O. André, M. Halvarsson, Atom probe tomography investigation of 3D nanoscale compositional variations in CVD TiAlN nanolamella coatings, *Surf. Coat. Technol.* 426 (2021), 127741.
- [15] L. von Fieandt, K. Johansson, T. Larsson, M. Boman, E. Lindahl, On the growth, orientation and hardness of chemical vapor deposited Ti(C,N), *Thin Solid Films* 645 (2018) 19–26.
- [16] J.G. Hulkko, K. Bőör, R. Qiu, O. Bäcke, M. Boman, M. Halvarsson, E. Lindahl, Kinetics of the low-pressure chemical vapor deposited tungsten nitride process using tungsten hexafluoride and ammonia precursors, *J. Vac. Sci. Technol. A* 39 (2021) 63403.
- [17] H. Euchner, P.H. Mayrhofer, Vacancy-dependent stability of cubic and wurtzite  $\text{Ti}_{1-x}\text{Al}_x\text{N}$ , *Surf. Coat. Technol.* 275 (2015) 214–218.
- [18] J. Todt, J. Zalesak, R. Daniel, R. Pitonak, A. Köpf, R. Weißenbacher, B. Sartory, C. Mitterer, J. Keckes, Al-rich cubic  $\text{Al}_{0.8}\text{Ti}_{0.2}\text{N}$  coating with self-organized nanolamellar microstructure: thermal and mechanical properties, *Surf. Coat. Technol.* 291 (2016) 89–93.
- [19] K. Bőör, R. Qiu, A. Forslund, O. Bäcke, H. Larsson, E. Lindahl, M. Halvarsson, M. Boman, L. von Fieandt, Chemical vapor deposition of TiN on a CoCrFeNi multi-principal element alloy substrate, *Surf. Coat. Technol.* 393 (2020), 125778.
- [20] M. Moreno, J.M. Andersson, R. Boyd, M.P. Johansson-Jöesaar, L.J.S. Johnson, M. Odén, L. Rogström, Crater wear mechanism of TiAlN coatings during high-speed metal turning, *Wear*. 484–485 (2021), 204016.
- [21] Z. Chen, J.M. Zhou, R.L. Peng, R. M'Saoubi, D. Gustafsson, F. Palmert, J. Moverare, Plastic deformation and residual stress in high speed turning of AD730TM nickel-based Superalloy with PCBN and WC tools, *Procedia CIRP*. 71 (2018) 440–445.
- [22] A. Hörling, L. Hultman, M. Odén, J. Sjölen, L. Karlsson, Mechanical properties and machining performance of  $\text{Ti}_{1-x}\text{Al}_x\text{N}$ -coated cutting tools, *Surf. Coat. Technol.* 191 (2005) 384–392.
- [23] I.C. Schramm, M.P. Johansson-Jöesaar, J. Jensen, F. Mücklich, M. Odén, Impact of nitrogen vacancies on the high temperature behavior of  $(\text{Ti}_{1-x}\text{Al}_x\text{N})_y$  alloys, *Acta Mater.* 119 (2016) 218–228.
- [24] L. von Fieandt, M. Fallqvist, T. Larsson, E. Lindahl, M. Boman, Tribological properties of highly oriented Ti(C,N) deposited by chemical vapor deposition, *Tribol. Int.* 119 (2018) 593–599.
- [25] M. Halvarsson, V. Langer, S. Vuorinen, Determination of the thermal expansion of  $\kappa\text{-Al}_2\text{O}_3$  by high temperature XRD, *Surf. Coat. Technol.* 76–77 (1995) 358–362.
- [26] C. Ruberto, Y. Yourdshahyan, B.I. Lundqvist, Surface properties of metastable alumina: a comparative study of  $\kappa$ - and  $\alpha$ - $\text{Al}_2\text{O}_3$ , *Phys. Rev. B* 67 (2003), 195412.
- [27] Y. Yourdshahyan, C. Ruberto, M. Halvarsson, L. Bengtsson, V. Langer, B. I. Lundqvist, S. Ruppi, U. Rolander, Theoretical structure determination of a complex material:  $\kappa\text{-Al}_2\text{O}_3$ , *J. Am. Ceram. Soc.* 82 (1999) 1365–1380.
- [28] J.-S. Chun, I. Petrov, J.E. Greene, Dense fully 111-textured TiN diffusion barriers: enhanced lifetime through microstructure control during layer growth, *J. Appl. Phys.* 86 (1999) 3633–3641.
- [29] M. Ben Hassine, H.-O. André, A.H.S. Iyer, A. Lotsari, O. Bäcke, D. Stiens, W. Janssen, T. Manns, J. Kümmel, M. Halvarsson, Growth model for high-Al containing CVD TiAlN coatings on cemented carbides using intermediate layers of TiN, *Surf. Coat. Technol.* 421 (2021), 127361.
- [30] G. Abadias, Y.Y. Tse, Diffraction stress analysis in fiber-textured TiN thin films grown by ion-beam sputtering: application to (001) and mixed (001)+(111) texture, *J. Appl. Phys.* 95 (2004) 2414–2428.
- [31] N. Li, S.K. Yadav, X.-Y. Liu, J. Wang, R.G. Hoagland, N. Mara, A. Misra, Quantification of dislocation nucleation stress in TiN through high-resolution in situ indentation experiments and first principles calculations, *Sci. Rep.* 5 (2015) 15813.
- [32] H. Yu, M. Bahadori, G.B. Thompson, C.R. Weinberger, Understanding dislocation slip in stoichiometric rocksalt transition metal carbides and nitrides, *J. Mater. Sci.* 52 (2017) 6235–6248.
- [33] Y. Kumashiro, A. Itoh, T. Kinoshita, M. Sobajima, The micro-Vickers hardness of TiC single crystals up to 1500° C, *J. Mater. Sci.* 12 (1977) 595–601.
- [34] Y. Kumashiro, Y. Nagai, H. Katō, E. Sakuma, K. Watanabe, S. Misawa, The preparation and characteristics of ZrC and TaC single crystals using an r.f. floating-zone process, *J. Mater. Sci.* 16 (1981) 2930–2933.
- [35] D.J. Rowcliffe, G.E. Hollox, Plastic flow and fracture of tantalum carbide and hafnium carbide at low temperatures, *J. Mater. Sci.* 6 (1971) 1261–1269.
- [36] F.R. Chien, X.J. Ning, A.H. Heuer, Slip systems and dislocation emission from crack tips in single crystal TiC at low temperatures, *Acta Mater.* 44 (1996) 2265–2283.
- [37] D.K. Chatterjee, M.G. Mendiratta, H.A. Lipsitt, Deformation behaviour of single crystals of titanium carbide, *J. Mater. Sci.* 14 (1979) 2151–2156.
- [38] D.W. Lee, J.S. Haggerty, Plasticity and creep in single crystals of zirconium carbide, *J. Am. Ceram. Soc.* 52 (1969) 641–647.
- [39] D.G. Sangiovanni, L. Hultman, V. Chirita, Supertoughening in B1 transition metal nitride alloys by increased valence electron concentration, *Acta Mater.* 59 (2011) 2121–2134.
- [40] R.M. Harris, P.D. Bristowe, Computer modelling of slip in TiC, *Philos. Mag. A* 79 (1999) 705–721.
- [41] F. Bachmann, R. Hielscher, H. Schaeben, Texture analysis with MTEX – free and open source software toolbox, *Solid State Phenom.* 160 (2010) 63–68.
- [42] E. Schmid, W. Boas, *Plasticity of Crystals*, with Special Reference to Metals, Springer, US, New York, 1968.
- [43] S.R. Agnew, Ö. Duygulu, Plastic anisotropy and the role of non-basal slip in magnesium alloy AZ31B, *Int. J. Plast.* 21 (2005) 1161–1193.
- [44] T. Li, T. Liu, L. Zhang, T. Fu, H. Wei, First-principles investigation on slip systems and twinnability of TiC, *Comput. Mater. Sci.* 126 (2017) 103–107.
- [45] W.S. Williams, Influence of temperature, strain rate, surface condition, and composition on the plasticity of transition-metal carbide crystals, *J. Appl. Phys.* 35 (1964) 1329–1338.
- [46] S.K. Yadav, R. Ramprasad, A. Misra, X.-Y. Liu, Core structure and Peierls stress of edge and screw dislocations in TiN: a density functional theory study, *Acta Mater.* 74 (2014) 268–277.
- [47] R. Peierls, The size of a dislocation, *Proc. Phys. Soc.* 52 (1940) 34–37.